IOP Publishing Journal of Optics
J. Opt. 18 (2016) 025702 (11pp) doi:10.1088/2040-8978/18/2/025702

Optimal broadband Mueller matrix ellipsometer using multi-waveplates with flexibly oriented axes

Honggang Gu[1], Xiuguo Chen[1,3], Hao Jiang[1], Chuanwei Zhang[1,2] and Shiyuan Liu[1,2,3]

[1] State Key Laboratory of Digital Manufacturing Equipment and Technology, Huazhong University of Science and Technology, Wuhan, Hubei 430074, People's Republic of China
[2] Wuhan Eoptics Technology Co. Ltd, Wuhan, Hubei 430075, People's Republic of China

E-mail: xiuguochen@hust.edu.cn and shyliu@hust.edu.cn

Received 16 October 2015, revised 2 December 2015
Accepted for publication 14 December 2015
Published 19 January 2016

Abstract

Accurate measurement of the Mueller matrix over a broad band is highly desirable for the characterization of nanostructures and nanomaterials. In this paper, we propose a general composite waveplate (GCW) that consists of multiple waveplates with flexibly oriented axes as a polarization modulating component in the Mueller matrix ellipsometer (MME). Although it is a common practice to make achromatic retarders by combining multiple waveplates, the novelty of the GCW is that both the retardances and azimuths of fast axes of the single-waveplates in the GCW are flexible parameters to be optimized, which is different from the conventional design where single-waveplates are usually arranged in symmetrical layout or with their fast axes parallel or perpendicular to each other. Consequently, the GCW can provide many more flexibilities to adapt to the optimization of the MME over a broad band. A quartz triplate, as a concrete example of the GCW, is designed and used in a house-made MME. The experimental results on the air demonstrate that the house-made MME using the optimally designed quartz triplates has an accuracy better than 0.2% and a precision better than 0.1% in the Mueller matrix measurement over a broad spectral range of 200~1000 nm. The house-made MME exhibits high measurement repeatability better than 0.004 nm in testing a series of standard SiO_2/Si samples with nominal oxide layer thicknesses ranging from 2 nm to 1000 nm.

Keywords: broadband Mueller matrix ellipsometer, general composite waveplate, optimal design, polarization

(Some figures may appear in colour only in the online journal)

1. Introduction

Mueller matrix ellipsometer (MME) has been developed as a powerful tool for nanoscale characterization [1–4]. Compared with conventional ellipsometers, MME can acquire much more information about the sample by providing all 16 elements of the 4 × 4 Mueller matrix in each measurement. Consequently, MME exhibits strong adavantages in characterizing anisotropic samples, especially nanostructures containing noticeable depolarization effects, etching anisotropy and asymmetric profiles [5–7], which can not be characterized using conventional ellipsometers. Over the past years, with the development of nanoscience and nanotechnology, various nanostructures and nanomaterials with inhomogeneity, anisotropy, rough surfaces and features, small size and unconventional shapes have been fabricated [8]. To characterize the profile parameters and optical properties of these emerging nanostructures and nanomaterials, Mueller matrix measurements with high accuracy and precision over a broad band especially covering the ultraviolet (UV) spectral range are fairly desired.

[3] Authors to whom any correspondence should be addressed.

Among the various types of MME, three configurations with the polarization modulated by dual-rotating retarder (DRR) [9–12], liquid crystal retarder (LCR) [13, 14], or photoelastic modulator (PEM) [15, 16] are the most commonly used. LCRs including ferroelectric liquid crystal retarders and liquid crystal variable retarders modulate the polarized light by changing the molecule orientations driven by external voltage. LCR-MMEs are more suitable for imaging and space applications due to the stable and non-resonant modulation without mechanical moving parts. However, they are difficult or even impossible to use in the UV range due to the serious absorption of the liquid crystal materials. PEMs are also driven by external voltage to modulate the polarized light based on the photoelastic effect [17]. By using four coupled PEMs, the complete Mueller matrix can be obtained with high speed over a broad band. The PEM-MMEs are the best choice for high sensitivity applications due to the high modulation purity and efficiency, broad spectral range and high retardance stability [16, 17]. However, the phase retardance of the PEM depends on both the voltage and the wavelength. It needs close control of the modulation amplitude as a function of wavelength, which thereby complicates the system significantly [18]. In addition, the data analysis of the PEM-MME is considerably complex due to the time-dependent irradiance produced by the oscillated retardance [15, 16, 18].

Compared with the PEM-MME and LCR-MME, the DRR-MME remains a relatively popular configuration due to its great potential for broadband operation, low complexity for alignment and calibration, and friendly manner for imaging [19–21]. The optical retarder is the key component of the DRR-MME to modulate the polarized light, whose applicable wavelength range limits the final operating spectral range of the ellipsometer. The typical retarders include waveplates and Fresnel prisms. Fresnel prisms can provide almost perfect achromatic retardance over a wide spectral range [22, 23]. However, they introduce relative attenuation between the two orthogonal polarized components of the polarized light, which thereby leads to considerable complexity and error sources to the system [23]. In addition, they usually have small apertures and need delicate mechanical alignment and adjustment to ensure their optical performances [14, 22]. Biplate and its alternatives, such as monoplate and Berek plate, are the most common waveplate retarders used in DRR-MMEs [3, 20]. However, their applicable spectral ranges are too narrow to be used in a broad band due to the strong dispersive effect. To minimize the dispersive effect and broaden the applicable spectral range, composite waveplates consisting of two or more single-waveplates are designed as achromatic or superachromatic retarders. One typical kind of achromatic waveplates is the Pancharatnam waveplate, which consists of three single-waveplates made from the same material with a symmetrical layout, namely, the first and last single-waveplates have identical retardances and are aligned with their fast axes parallel to each other but both are at an angle to that of the central half-wave plate [24]. Another type of achromatic waveplates is Beckers' waveplate, which is made of two or more single-waveplates with different materials and by fixing their fast axes parallel or perpendicular to each other [25, 26]. The superachromatic waveplate can be regarded as an extension of the Pancharatnam waveplate by replacing its single-waveplates with Beckers' waveplates [27]. However, these achromatic/superachromatic waveplates are limited to specific structures to construct linear retarders, which not only significantly sacrifice the flexibility to adapt to optimal broadband measurements of the MME, but also make them too complicate to be fabricated. In addition, these waveplates are usually designed as quarter/half-wave retarders, which not necessarily provide the optimal retardance for a DRR-MME [19].

In this work, we propose a general composite waveplate (GCW) that consists of multiple single-waveplates to be used as a polarization modulating component in MME. The novelty of the GCW is that both the retardances and azimuths of fast axes of the single-waveplates in the GCW are flexible parameters to be optimized, which is different from the conventional design of achromatic waveplates where single-waveplates are usually arranged in symmetrical layout or with their fast axes parallel or perpendicular to each other. The GCW is thereby not limited to specific structures, and consequently will provide many more flexibilities to adapt to the optimization of the MME over a broad band. In addition, compared to Fresnel retarders, it has a compact size, negligible relative attenuation, and low complexity to adjust. We construct an optical model based on Jones' equivalent theorem to describe the GCW [28]. Then we present the basic principles for data reduction and system calibration of a novel MME configuration using two rotating GCWs. A condition number related method is utilized to optimize the system configuration of the ellipsometer over a broad spectral range. The optimal design results of a quartz triplate for the MME covering the spectral range of 200∼1000 nm are presented as a concrete example to verify the proposed method. A house-made MME prototype based on the optimally designed quartz triplates has been developed to perform the experiments. Experimental results on the air demonstrate that the house-made MME has an accuracy better than 0.2% and a precision better than 0.1% in the Mueller matrix elements over the spectral range of 200∼1000 nm. The measurement repeatability is better than 0.004 nm in testing the thicknesses of a series of standard SiO_2/Si samples with nominal oxide layer thicknesses ranging from 2 nm to 1000 nm, demonstrating the house-made MME exhibits stable high-performances in characterizing both thin and thick thin films.

2. Theory

2.1. Modeling of GCW

A single-waveplate is a slice of birefringent crystal usually cut with the optic axis lying on the plane of the plate, and can be treated as a linear retarder. The effects of a single-waveplate on the polarized light can be represented by a 2 × 2 Jones

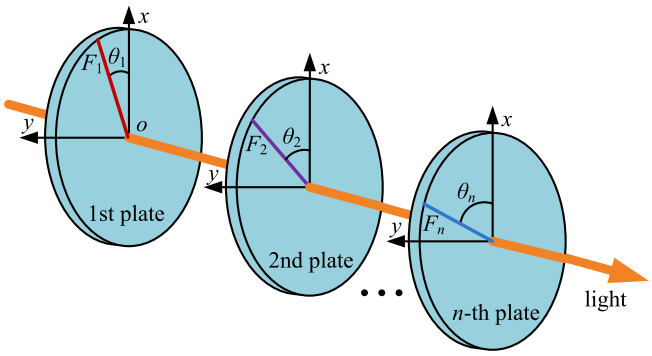

Figure 1. Schematic of a GCW. (F_i, θ_i) (i = 1, 2, …, n) refer to the fast axis of the i-th single-waveplate and its azimuth angle with respect to the x-axis, respectively.

matrix given by

$$\mathbf{J}(\delta) = \begin{bmatrix} e^{i\delta/2} & 0 \\ 0 & e^{-i\delta/2} \end{bmatrix}, \tag{1}$$

where δ is the retardance of the single-waveplate and can be calculated by

$$\delta = \frac{2\pi}{\lambda}\Delta n \cdot d, \tag{2}$$

where $\Delta n = (n_e - n_o)$ is the birefringence of the crystal, n_e and n_o denote the extraordinary and the ordinary refractive indices, d and λ refer to the thickness of the waveplate and the vacuum wavelength, respectively.

If we study the waveplate in a cartesian coordinate system and take the azimuth of the fast axis into account, the Jones matrix of the waveplate can be modified as

$$\mathbf{J}(\delta, \theta) = \mathbf{R}(-\theta)\mathbf{J}(\delta)\mathbf{R}(\theta), \tag{3}$$

where θ is the azimuthal angle of the fast axis with respect to the x-axis, and $\mathbf{R}(\alpha)$ is the Jones rotation matrix under a rotation angle α and is given by

$$\mathbf{R}(\alpha) = \begin{bmatrix} \cos\alpha & \sin\alpha \\ -\sin\alpha & \cos\alpha \end{bmatrix}. \tag{4}$$

A GCW can be treated as an optical system consisting of two or more single-waveplates. As schematically shown in figure 1, we again study the GCW in the cartesian coordinate system, and the light propagates along the z-axis and perpendicularly to the plane of the waveplate. The single-waveplates are numbered as 1, 2, …, n in the order of light propagation. Furthermore, let (d_i, θ_i) denote the thickness and the fast axis azimuth of the i-th single-waveplate, respectively. The retardance of the i-th waveplate δ_i can be calculated by equation (2). Thus the effect of the GCW on the polarized light can be calculated by

$$\mathbf{U} = \mathbf{J}(\delta_n, \theta_n)\cdots\mathbf{J}(\delta_2, \theta_2)\mathbf{J}(\delta_1, \theta_1) = \begin{bmatrix} u_{11} & u_{12} \\ u_{21} & u_{22} \end{bmatrix}, \tag{5}$$

where $\mathbf{J}(\delta_i, \theta_i)$ is the Jones matrix of the i-th waveplate calculated by equation (3). The matrix $\mathbf{U}$ is unitary, and the relations of its elements are

$$u_{22} = u_{11}^*, \; u_{21} = -u_{12}^*. \tag{6}$$

where the notation '*' represents the complex conjugate of a complex number.

According to Jones' equivalent theorem, the GCW can be optically equivalent to a cascaded system containing a pure retarder and a rotator [28]. Therefore, the Jones matrix of the GCW can be described as

$$\mathbf{U} = \mathbf{R}(\rho_e)\mathbf{R}(-\theta_e)\mathbf{J}(\delta_e)\mathbf{R}(\theta_e) = \mathbf{R}(\rho_e)\mathbf{J}(\delta_e, \theta_e), \tag{7}$$

where (δ_e, θ_e) are the equivalent retardance and the equivalent fast axis azimuth of the resulting retarder, and ρ_e is the rotary angle of the resulting rotator. In a polarization system, the polarization rotator rotates the polarization plane of the polarized light by a certain angle, i.e., the rotary angle of the rotator, while the retarder introduces a phase shift named the retardance between the two orthogonal components of the polarized light along with the directions parallel and perpendicular to the fast axis of the retarder. In the GCW, the retardance and the rotary angle are the intrinsic properties of the retarder and the rotator, respectively, and they are determined only by the nature of the single-waveplates and their relative orientations. While the equivalent fast axis azimuth of the retarder defines the orientation of the optical system (i.e., the train of the single-waveplates), it depends not only on the structure of the GCW, but also on the global orientation of the system with respect to the coordinate.

Combining equations (7) and (5), we can derive the expressions for the equivalent parameters of the GCW that are given by [29]

$$\delta_e = 2\tan^{-1}\left[\sqrt{\frac{\mathrm{Im}^2(u_{11}) + \mathrm{Im}^2(u_{12})}{\mathrm{Re}^2(u_{11}) + \mathrm{Re}^2(u_{12})}}\right], \tag{8a}$$

$$\theta_e = \frac{1}{2}\tan^{-1}\left[\frac{\mathrm{Re}(u_{11})\mathrm{Im}(u_{12}) + \mathrm{Im}(u_{11})\mathrm{Re}(u_{12})}{\mathrm{Re}(u_{11})\mathrm{Im}(u_{11}) - \mathrm{Re}(u_{12})\mathrm{Im}(u_{12})}\right], \tag{8b}$$

$$\rho_e = \tan^{-1}\left[\frac{\mathrm{Re}(u_{12})}{\mathrm{Re}(u_{11})}\right]. \tag{8c}$$

2.2. Working principles

As schematically shown in figure 2, the basic system layout of the MME using two rotating GCWs in the order of light propagation is $PW_{r1}(\omega_1)SW_{r2}(\omega_2)A$, where P and A stand for the polarizer and analyzer, W_{r1} and W_{r2} refer to the 1st and 2nd frequency-coupled rotating GCWs, and S stands for the sample. The Stokes vector S_{out} of the exiting light beam can be expressed as the following Mueller matrix product

$$\begin{aligned}\mathbf{S}_{out} = &[\mathbf{M}_A\mathbf{R}(A)][\mathbf{R}(\rho_{e2})\mathbf{R}(-\theta_{e2})\mathbf{M}_{W_{r1}}(\delta_{e2}) \\ &\times \mathbf{R}(\theta_{e2})]\mathbf{M}_s[\mathbf{R}(\rho_{e1})\mathbf{R}(-\theta_{e1}) \\ &\times \mathbf{M}_{W_{r1}}(\delta_{e1})\mathbf{R}(\theta_{e1})][\mathbf{R}(-P)\mathbf{M}_P]\mathbf{S}_{in},\end{aligned} \tag{9}$$

where $\mathbf{M}_i$ (i = P, A, W_{r1}, W_{r2}, S) is the Mueller matrix associated with each optical element, and $\mathbf{R}(\alpha)$ is the Mueller rotation transformation matrix for rotation by the angle α. P and A are the transmission axis azimuths of the polarizer and

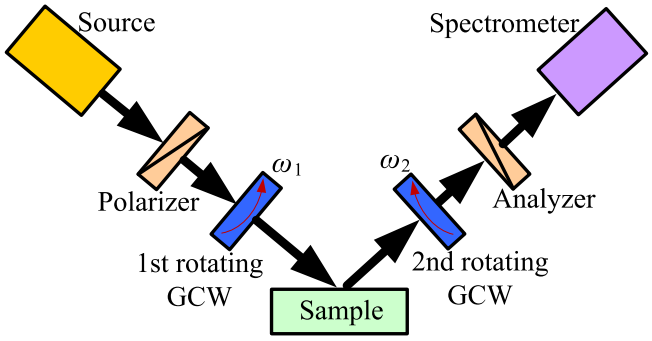

Figure 2. Schematic of the MME based on GCWs.

the analyzer with respect to the incident plane, and (δ_{e1}, θ_{e1}, ρ_{e1}) and (δ_{e2}, θ_{e2}, ρ_{e2}) are the equivalent retardance, the equivalent fast axis azimuth and the equivalent rotary angle of the 1st rotating GCW and those of the 2nd rotating GCW, respectively. Since the retardances and the rotary angles depend only on the structure of GCWs, they remain unchanged during the rotation. While the fast axis azimuths change continuously with the rotation of the GCWs and produce modulation of the polarized light, i.e., $\theta_{e1} = \omega_1 t - \theta_{e10}$, $\theta_{e2} = \omega_2 t - \theta_{e20}$, where $\omega_1 = m_1\omega$, $\omega_2 = m_2\omega$, m_1 and m_2 are positive integers and ω is the fundamental mechanical frequency, and θ_{e10} and θ_{e20} denote the original fast axis azimuths of the 1st and 2nd rotating GCWs (i. e. at the time $t = 0$).

Thus, equation (9) can be rearranged as

$$\begin{aligned}\mathbf{S}_{out} &= [\mathbf{M}_A\mathbf{R}(A + \rho_{e2})][\mathbf{R}(-\theta_{e2})\mathbf{M}_{W_{r2}}(\delta_{e2}) \\ &\quad \times \mathbf{R}(\theta_{e2})]\mathbf{M}_s[\mathbf{R}(\rho_{e1} - \theta_{e1})\mathbf{M}_{W_{r1}}(\delta_{e1}) \\ &\quad \times \mathbf{R}(\theta_{e1} - \rho_{e1})][\mathbf{R}(\rho_{e1} - P)\mathbf{M}_P]\mathbf{S}_{in} \\ &= [\mathbf{M}_A\mathbf{R}(A')][\mathbf{R}(-\theta'_{e2})\mathbf{M}_{W_{r2}}(\delta_{e2}) \\ &\quad \times \mathbf{R}(\theta'_{e2})]\mathbf{M}_s[\mathbf{R}(-\theta'_{e1})\mathbf{M}_{W_{r1}}(\delta_{e1})\mathbf{R}(\theta'_{e1})] \\ &\quad \times [\mathbf{R}(-P')\mathbf{M}_P]\mathbf{S}_{in}. \end{aligned} \tag{10}$$

where $A' = A + \rho_{e2}$, $P' = P - \rho_{e1}$, $\theta'_{e1} = \omega_1 t - \theta'_{e10}$, $\theta'_{e2} = \omega_2 t - \theta'_{e20}$, $\theta'_{e10} = \theta_{e10} + \rho_{e1}$, $\theta'_{e20} = \theta_{e20}$. In contrast to the conventional DRR-MME [10], the GCW-based MME contains two linear retarders as well as two additional rotators introduced by the GCWs. The azimuths of the linear retarders rotate synchronously at ω_1 and ω_2, while the retardances of the linear retarders and the rotary angles of the rotators will remain unchanged when the GCWs continuously rotate, which can be easily confirmed from equation (8). Moreover, the rotary angles can be incorporated into the original azimuths of the polarizer, analyzer and retarders as shown in equation (10).

The irradiance at the detector is proportional to the first element of S_{out}, which can be obtained by multiplying the matrices in equation (10). Thus the system model of the presented MME can be formulated as [30]

$$\mathbf{G} = \mathbf{D}(\mathbf{b}) \cdot \mathbf{M}, \tag{11}$$

where $\mathbf{G}$ is a K-element flux vector of irradiance measured by the detector, $\mathbf{D}$ is a $K \times 16$ instrument matrix, which is a function of a system-dependent vector $\mathbf{b}$, and $\mathbf{M}$ is the Mueller matrix of the sample that has been flattened into a 16-element vector. The variables in $\mathbf{b}$ include the transmission axis azimuths of the polarizer and analyzer, the original fast axis azimuths, the rotary angles, and the retardances of the two GCWs etc. i.e., $\mathbf{b} = [P, A, \theta_{e10}, \theta_{e20}, \rho_{e1}, \rho_{e2}, \delta_{e1}, \delta_{e2}, \ldots]^T$. Since the rotary angles are not independent parameters, the vector $\mathbf{b}$ can be simplified as $[P', A', \theta'_{e10}, \theta'_{e20}, \delta_{e1}, \delta_{e2}, \ldots]^T$. Thus, the Mueller matrix of the sample can be extracted by

$$\mathbf{M} = \mathbf{D}(\mathbf{b})^+\mathbf{G}, \tag{12}$$

where $\mathbf{D}^+ = [\mathbf{D}^T\mathbf{D}]^{-1}\mathbf{D}^T$ is the Moore–Penrose pseudo-inverse matrix of $\mathbf{D}$.

The systematic parameters in $\mathbf{b}$ of the MME system must be accurately determined before performing sample measurements. These parameters can be obtained by performing a system calibration procedure as described as

$$\hat{\mathbf{b}} = \arg\min_{\mathbf{b}\in\Theta} \|\mathbf{D}(\mathbf{b}) - \hat{\mathbf{D}}\|_F, \tag{13}$$

where $\hat{\mathbf{b}}$ is the vector of the calibrated systematic parameters, Θ is the domain for these systematic parameters, $\hat{\mathbf{D}}$ is the measured instrument matrix of a standard calibration sample, and the subscript F refers to the F-norm of a matrix.

2.3. Optimization metric

In practice, the measurements invariably have uncertainties associated with the detected intensities $\mathbf{G}$ and the instrument matrix $\mathbf{D}$. Meanwhile, the MME can be operated under different configurations (i.e., system-dependent vector $\mathbf{b}$), which have different sensitivities to the errors. Various metrics have been designed to optimize the configurations for ellipsometers or polarimeters, including metrics related to condition number and the determinant [19, 21, 31]. The optimization aims to equalize the range of singular values of the instrument matrix so that the basis vectors have wide distribution and similar weight, and to ensure the detected states span the space of the polarization states of the polarized light beam as well as make it possible to improve the immunity of the system to the errors. In this paper, we use the condition number of the instrument matrix $\mathbf{D}$ as the metric to optimize the ellipsometer, which is defined as

$$\kappa = \|\mathbf{D}\|_p \cdot \|\mathbf{D}^+\|_p, \tag{14}$$

where the notation $\|\mathbf{D}\|_p$ represents the p-norm of $\mathbf{D}$, and p can be 1, 2 or ∞.

The objective of the optimal design is to obtain sets of systematic parameters $\mathbf{b}$ to minimize κ in order to reduce the influences of errors on the measurements. Since the azimuths of the polarizer and analyzer have negligible effects on the condition number [19], they can be fixed in the optimization. The remaining parameters in $\mathbf{b}$ are all introduced by the GCWs. Although these parameters are strongly wavelength-dependent, they can be determined by the thicknesses and the fast axis azimuths of the single-waveplates in the GCWs. For simplicity, we assume that the 1st and the 2nd rotating GCWs are identical, and that the single-waveplates of the GCWs are zero-order quarter waveplates. Then for each single-

waveplate, according to equation (2) we have

$$d = \frac{\lambda_0}{4\Delta n(\lambda_0)}, \tag{15a}$$

$$\delta(\lambda) = \frac{\pi}{2}\frac{\lambda_0}{\lambda}\frac{\Delta n(\lambda)}{\Delta n(\lambda_0)}, \tag{15b}$$

where λ_0 is the central wavelength for the quarter single-waveplate.

Under these conditions, the parameters to be optimized for a broadband MME are the central wavelengths and the fast axis azimuths of the single-waveplates. In this case, the criterion for the optimal design can be described as

$$(\boldsymbol{\lambda}_o, \boldsymbol{\theta}_o) = \arg \min_{(\boldsymbol{\lambda},\boldsymbol{\theta})\in\boldsymbol{\Lambda}} [\max_{\lambda\in\boldsymbol{\Gamma}} |\kappa(\lambda)|], \tag{16}$$

where $\boldsymbol{\lambda} = (\lambda_1, \lambda_2, \ldots, \lambda_n)$ and $\boldsymbol{\theta} = (\theta_1, \theta_2, \ldots, \theta_n)$ refer to the central wavelengths and fast axis azimuths of the single-waveplates, while $\boldsymbol{\lambda}_o = (\lambda_{1o}, \lambda_{2o}, \ldots, \lambda_{no})$ and $\boldsymbol{\theta}_o = (0_{1o}, \theta_{2o}, \ldots, \theta_{no})$ refer to the corresponding optimal values. $\boldsymbol{\Lambda}$ and $\boldsymbol{\Gamma}$ are the domain for the design parameters of the zero-order quarter single-waveplates and the domain for the applicable wavelength range of the target MME.

3. Design of GCWs

In this section, we present the optimal design process of the GCWs for the MME using the proposed method in details. The domain for the applicable wavelength range of the target MME is chosen as $\boldsymbol{\Gamma} = (0.2\ \mu\text{m}, 1\ \mu\text{m})$ covering the UV–vis-NIR wavelength range. The motor frequency ratio and the number of the flux are chosen to be $m_1{:}m_2 = 5{:}3$ and $K = 50$, respectively. Further we assume that the fast axes of the first single-waveplates of the GCWs are aligned parallel to the respect plane [i.e., $\theta_1(\text{W}_{r1}) = \theta_1(\text{W}_{r2}) = 0$]. In this paper, the 2-norm is utilized to calculate the condition number. Using equation (16) and the principles presented in section 2, we can carry out the optimal design of the GCWs for the MME.

Here, we show the optimally designed results of a triplate which contains three zero-order quarter waveplates made of quartz as an example. The central wavelengths and the azimuths of the single-waveplates in the optimally designed quartz triplate are (792.5 nm, 1014.3 nm, 705.1 nm) and (0°, 64.8°, 17.0°), respectively. To make a comparison, we present the results of a Pancharatnam waveplate [24] and a superachromatic waveplate [27], which are both optimized for the MME using a metric similar to equation (16) by minimizing the maximum of the condition number over the spectral range of 200∼1000 nm. The Pancharatnam waveplate consists of three single waveplates made from quartz, and the retardances of the 1st, 2nd and 3rd single-waveplates are 120.27°, 180° and 120.27° at the central wavelength 336.1 nm, and the angle between the axes of the 1st and 3rd single-waveplates and that of the 2nd single-waveplate is 50.86°. The superachromatic waveplate is also a Pancharatnam waveplate but with the elements replaced by quartz-MgF_2 achromatic waveplates for 200∼1000 nm, and the nominal retardances of the three achromatic waveplates are 142.02°, 180° and 142.02°, and the angle between the axes of the 1st and 3rd achromatic waveplates and that of the 2nd achromatic waveplate is 61.35°. The birefringences of the quartz and MgF_2 materials involved in this paper can be calculated by Sellmeier's equations [32, 33].

Figure 3 shows the condition number spectra of the corresponding MMEs based on optimally designed quartz triplate as well as the Pancharatnam waveplate and the superachromatic waveplate. It can be observed from figure 3 that the lowest condition number for this MME configuration is about 3.7. The maximum values of the condition number spectra are 7.4, 27.1 and 5.5 for the triplate, the Pancharatnam waveplate and the superachromatic waveplate, respectively. The condition number spectrum of the triplate is only slightly greater than that of the superachromatic waveplate, and is much better than that of the Pancharatnam waveplate. However, the presented triplate has the advantages over the superachromatic waveplate that it contains only three components and all the components are made from the same material. Thus, compared with the conventional achromatic and superachromatic waveplates, the presented GCWs are not limited to specific structures, and therefore provide much more flexibility to adapt to the optimization of the MME.

4. Instrumentation and calibration

4.1. Instrumentation

We developed an MME prototype, as depicted in figure 4. This instrumentation consists of a light source, a polarization state generator (PSG) arm, a sample stage, a polarization state analyzer (PSA) arm, and a detector. The PSG contains a collimator lens, a polarizer and a rotating GCW in the order of the light propagation, while the PSA contains a second rotating GCW, an analyzer and a focus lens. The light source and the detector are connected through optical fibers with the PSG and PSA, respectively.

The rotating GCWs used in the house-made MME are optimally designed quartz triplates. The components of the triplates are zero-order quarter waveplates made from quartz, and their design parameters have been presented in section 3. The thickness of a true zero-order quartz plate is only tens of microns that is too thin to be cut and polished. The common practice is to combine two thick plates with their fast axes aligned perpendicular to each other to make a compound zero-order waveplate. However, these compound zero-order waveplates will suffer from various artifacts due to the misalignment errors between the axes [20, 29]. To overcome these practical difficulties, the quartz crystal is cemented on the JGS1 optical glass substrate and then can be polished to true zero-order waveplates. After all the component single-waveplates are manufactured according to their designed central wavelengths, they are cemented together with their fast axes aligned at the optimal designed orientations. All the plates as well as the substrates directly contact each other without any air gap by using optical cement method, which reduces the interference effects and improves the

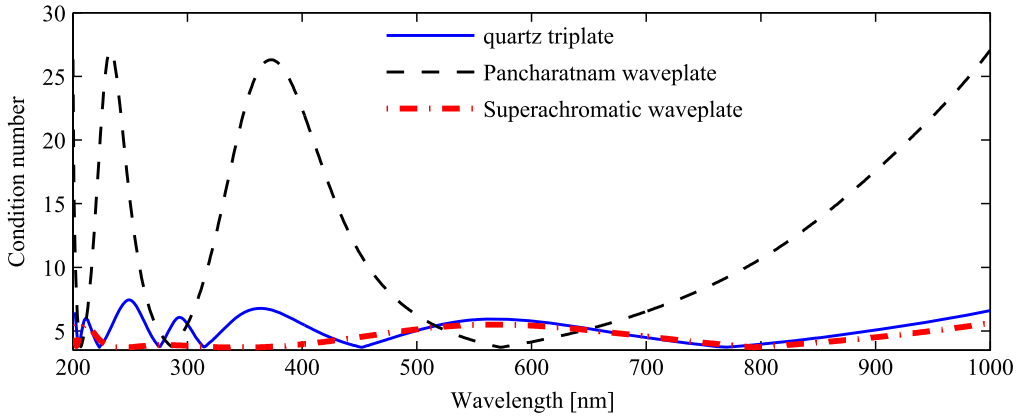

Figure 3. Condition number spectra of MMEs based on the optimally designed quartz triplate, Pancharatnam waveplate and superachromatic waveplate.

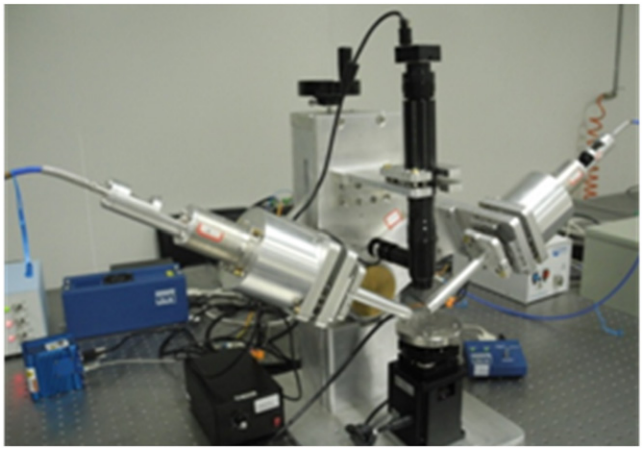

Figure 4. The house-made MME prototype using optimally designed quartz triplates.

transmittance of the polarized light. The triplates are protected in cylindrical mount engraved with the fast axis direction of the first single-waveplate.

In addition to the GCWs, other optical components have been attentively selected to ensure that the applicable wavelength range of the ellipsometer covers 200∼1000 nm. The light source is a deuterium and quartz-tungsten-halogen combined source from BWTEK, the polarizer and the analyzer are α-barium borate (α-BBO) Rochon prisms from Union Optic, and the detector is a custom made spectrometer from BWTEK, the collimator and the focuser are achromatic triplet lens and plano-convex lens from Edmund, and the fibers are UV anti-exposure fibers from Ocean Optics. The GCWs of the PSG and PSA are mounted on the hollow shaft motors (DRTM 40-D25-HiDS, Owis, Inc., Germany) and rotated continuously with angular speeds of 12.5π rad/s and 7.5π rad/s (i.e., ω_1:ω_2 = 5:3), respectively. Thus the fundamental mechanical rotation speed ω is 2.5π rad/s and the basic optical period of the MME is 0.4 s. The spectrometer has a wavelength resolution of 0.5 nm and the integration time is set as 8 ms so that we can obtain 50 integrals of the irradiance over the fundamental optical period (i.e., $K = 50$).

With the house-designed triplates and the selected components, the MME experimental platform is set up. In construction of the ellipsometer, the azimuths of the transmission axes of the polarizer and analyzer as well as those of engraved lines of the triplates are tried to be set at 0° with respect to the incident plane. Two measurement modes, named as the straight-through measurement mode and the reflective measurement mode, can be chosen by rotating the two polarization state arms (i. e., PSG and PSA) of the ellipsometer in experiments.

4.2. System calibration

The systematic parameters of the ellipsometer, including the retardances, the original fast axis azimuths and the rotary angles of the GCWs, and the original orientations of the transmission axis of the polarizer and analyzer, must be determined before performing measurements. As described in section 2.2, the independent parameters to be calibrated can be reduced to $\mathbf{b} = [P', A', \theta'_{e10}, \theta'_{e20}, \delta_{e1}, \delta_{e2}, \ldots]^T$, where $P' = P - \rho_{e1}$ is the azimuth of the polarizer incorporating the rotary angle of the first GCW, $A' = A + \rho_{e2}$ is the azimuth of the analyzer incorporating the rotary angle of the second GCW, $\theta'_{e10} = \theta_{e10} + \rho_{e1}$ is the effective fast axis azimuth of the first GCW incorporating the rotary angle of the first GCW, $\theta'_{e20} = \theta_{e20}$ is the effective fast axis azimuth of the second GCW, and δ_{e1} and δ_{e2} are the effective retardances of the first and the second GCWs. If the azimuths of the transmission axes of the polarizer and analyzer as well as those of engraved lines of the GCWs are set at 0°, then there will be $P' = -\rho_{e1}$, $A' = \rho_{e2}$, $\theta'_{e10} = \theta_{e10} + \rho_{e1}$, $\theta'_{e20} = \theta_{e20}$.

These systematic parameters can be obtained by performing a regression calibration procedure using a standard calibration sample as shown in equation (13) [34]. In this paper, the system calibration is performed at the reflective measurement mode with an incident angle of 60° using a SiO_2 film on Si substrate with a nominal thickness of 100 nm as the standard calibration sample. Since all the systematic parameters are strongly wavelength-dependent due to the dispersive effect of the quartz crystal, the regression calibration procedure is performed in a wavelength-by-wavelength way

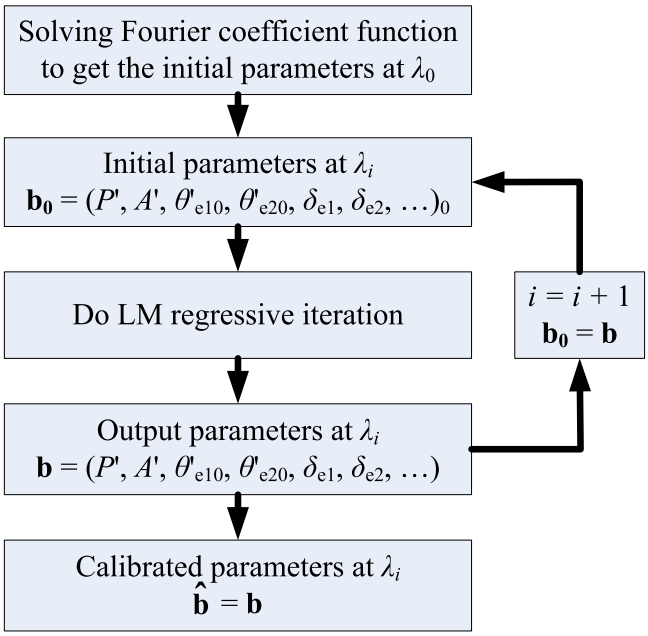

Figure 5. Flowchart of the wavelength-by-wavelength regression calibration procedure.

as shown in figure 5. Firstly, we obtain the initial values of the systematic parameters for the first wavelength of the concerned wavelength range by solving the Fourier coefficient functions [10, 20]. Then, with the given initial values of the systematic parameters, a regressive iteration based on LM algorithm is performed to obtain the final values for these parameters. The output parameters of the LM iteration are treated as the final calibrated parameters for the current wavelength and the initial parameters for the next wavelength. At last, the system calibration can be completed by repeating the above regressive iteration wavelength-by-wavelength.

The calibrated parameters as well as the experimental condition number spectra are shown in figure 6 compared with the designed spectra of the triplate. It can be observed from figure 6 that the rotary angles of the first and second triplates have been incorporated into the azimuths of the first triplate and the polarizer and that of the analyzer, respectively, which agrees with the theoretical relations presented in section 2.2. Although the systematic parameters including the retardances and the azimuths are highly dispersive, they provide a relative well-conditioned MME system over the experimental spectral range. The calibrated spectra of the ellipsometer demonstrate high agreement with the designed ones. Differences in the spectra especially in UV spectral range are due to fabrication errors in thicknesses and alignment of single-waveplates. Although the GCWs are equally designed, the thickness error in polishing the single-waveplate can be several hundred nanometers, which further results in a maximum deviation of ten to twenty nanometers in the central wavelength of the single-waveplate. These errors make the spectra of the practical GCWs different from each other especially in the UV range. Fortunately, the GCWs produce relatively good condition number spectra when the deviations in the retardances from their designed values are controlled as the current error level in fabrication.

5. Results and discussion

In this section, we present the experimental results performed on the house-made MME, including the measurement results of the air and a series of SiO_2 thin films grown on the Si substrate with the nominal thicknesses ranging from 2 nm to 1000 nm. These results are used to evaluate the performances of the ellipsometer, including the measurement accuracy and precision of the Mueller matrix, and the measurement repeatability of the thickness for SiO_2 thin films.

It is customary to evaluate the performance of an MME by measuring the Mueller matrix of the air which is an identity matrix. In this paper, we use the mean bias and the standard deviation of air's Mueller matrix elements to define the measurement accuracy and precision of the ellipsometer as given by

$$\Delta(m_{i,j}) = \frac{1}{L}\sum_{l=1}^{L}(m_{ij}^{l} - m_{ij}^{0}), \tag{17a}$$

$$\sigma(m_{i,j}) = \sqrt{\frac{1}{L}\sum_{l=1}^{L}(m_{ij}^{l} - m_{ij}^{0})^2}, \tag{17b}$$

where $m_{ij} = M_{ij}/M_{11}$ $(i, j = 1, 2, 3, 4)$ refers to the normalized Mueller matrix element, m^{l}_{ij} and m^{0}_{ij} denote normalized Mueller matrix elements of the l-th measurement and those of the ideal air respectively, and L is the total number of measurements.

Measurement deviations in the Mueller matrix originate from two categories of errors, i.e., systematic errors and random noises. Systematic errors come from the residual errors in the calibrated systematic parameters and they mainly affect the measurement accuracy, while random errors may come from noises in the light source, the motor modulation, the spectrometer and the environment, and they mainly have influences on the measurement precision. Besides, these measurement deviations are also affected by the immunity of the system. In order to investigate the measurement accuracy and precision of the house-made ellipsometer, 30 repeated measurements on Mueller matrix of the air are made at the straight-through measurement mode. Figure 7 depicts the mean bias and the standard deviation in the Mueller matrix elements of the measurements.

It can be observed from figure 7 that the absolute mean biases in the Mueller matrix elements are less than 0.001 over most of the spectral range, and they are never larger than 0.002, and the standard deviations of the Mueller matrix elements are less than 0.001 over the whole experimental spectral range. Thus, the measurement accuracy and measurement precision of the house-made MME are better than 0.2% and 0.1%, respectively. In addition, the measurement deviations have quite well-balanced distribution in the Mueller matrix elements over the whole spectral range, which demonstrates the house-made MME is designed with well-conditioned immunity to the errors. It can be seen from

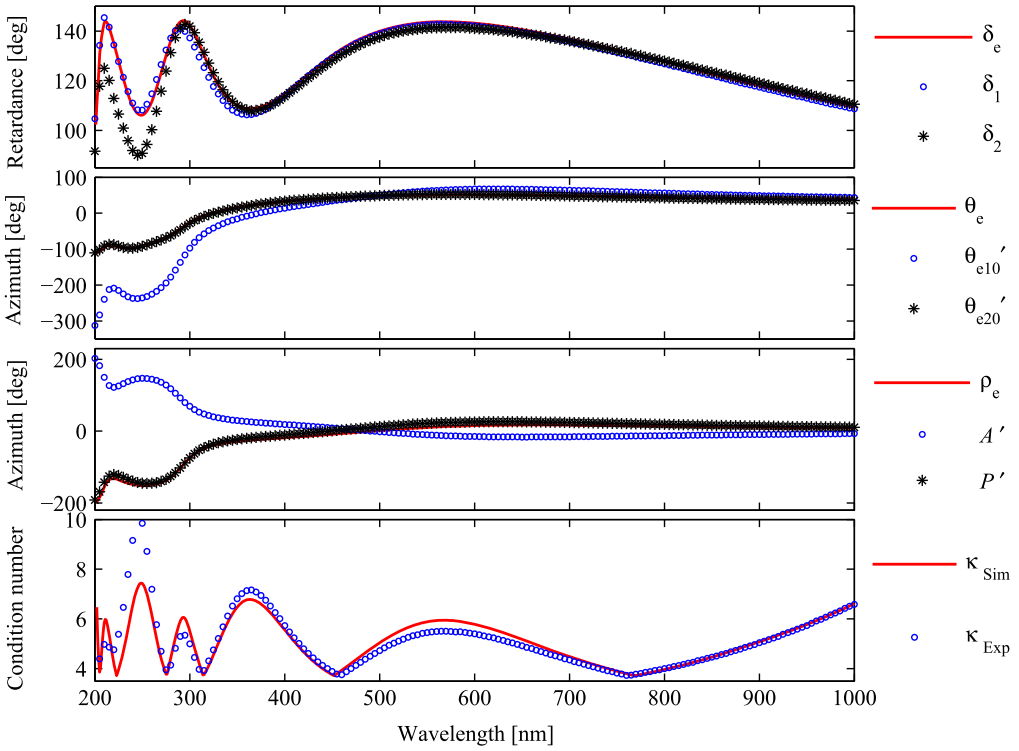

Figure 6. Calibrated systematic parameters and the experimental condition number of the MME compared with the designed spectra of the corresponding quartz triplate. (δ_e, θ_e, ρ_e) denote the optimally designed results for the equivalent retardance and the equivalent fast axis azimuth and the equivalent rotary angle of the triplate, (δ_1, δ_2) are the calibrated retardances for the first and the second triplates, (P', A') are the calibrated azimuth of the polarizer incorporating the rotary angle of the first triplate and the calibrated azimuth of the analyzer incorporating the rotary angle of the second triplate, (θ'_{e10}, θ'_{e20}) are the fast axis azimuth of the first triplate incorporating the rotary angle of the first triplate and the fast axis azimuth of the second triplate, and (κ_{sim}, κ_{exp}) are the simulated and experimental condition numbers for the MME based on quartz triplates.

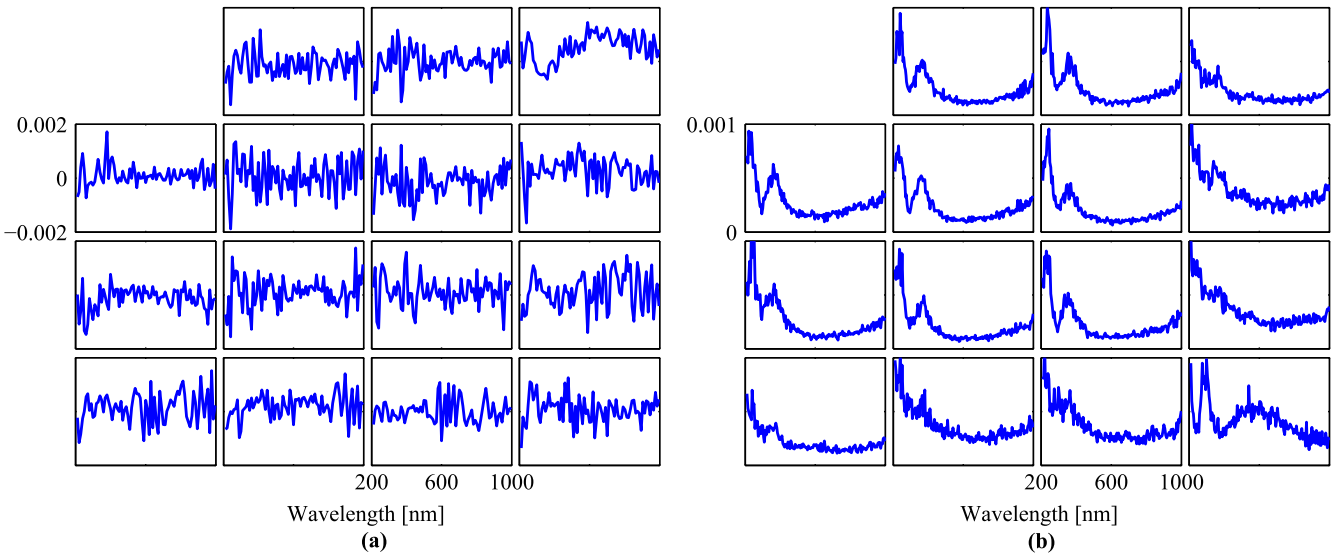

Figure 7. Results of 30 repeated measurements on the air performed on the house-made MME: (a) Mean bias in the Mueller matrix elements; (b) Standard deviation in the Mueller matrix elements. The horizontal axes, varying from 200 to 1000 nm with an increment of 5 nm, denote the wavelengths, and the vertical axes for (a), varying from −0.002 to 0.002, denote the mean bias in the associated Mueller matrix elements, and for (b), varying from 0 to 0.001, denote the standard deviation in the associated Mueller matrix elements. The mean bias and the standard deviation are estimated by 30 repeated measurements.

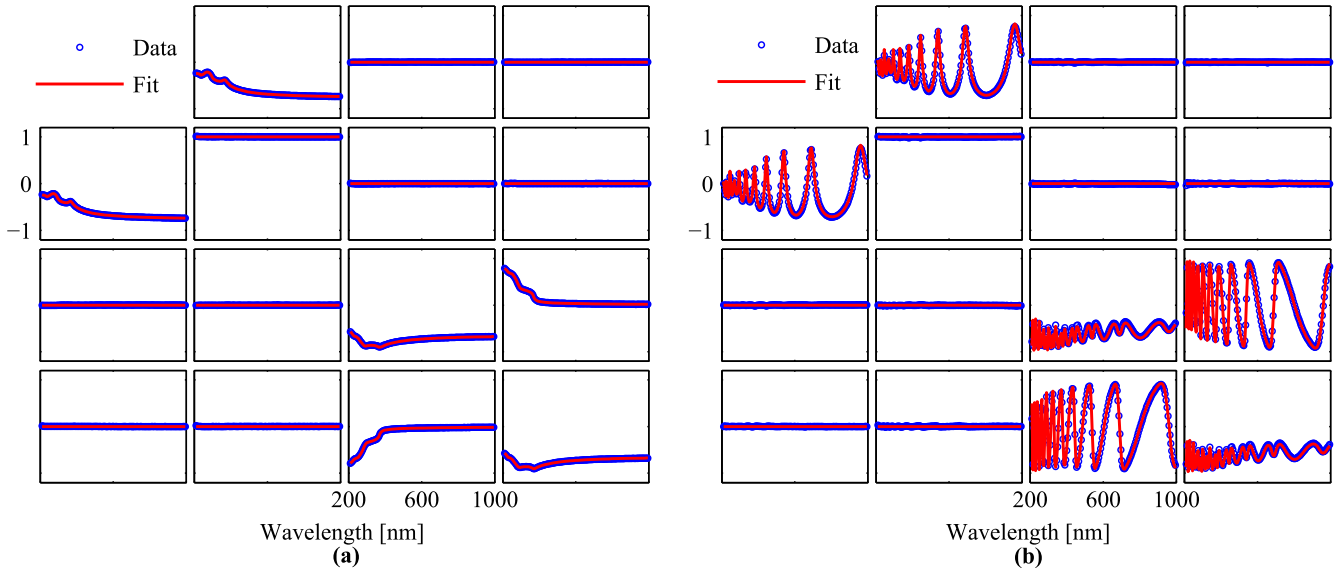

Figure 8. (a) Fitting results of the measured and calculated best-fit Mueller matrix spectra of the 2 nm SiO_2 film; (b) Fitting results of the measured and calculated best-fit Mueller matrix spectra of the 1000 nm SiO_2 film. The horizontal axes, varying from 200 to 1000 nm with an increment of 5 nm, denote the wavelengths, and the vertical axes, varying from −1.1 to 1.1, denote the normalized Mueller matrix elements.

figure 7(b) that the standard deviation spectra show approximate trends with the condition number spectrum, which demonstrates the effectiveness of the condition number metric in evaluating the immunity of the system to the errors. Differences in the trends may be caused by the different relative noise level over the spectrum. Weak light intensity and poor response of the spectrometer result in a high relative noise level, and that is why the standard deviations in the Mueller matrix are relatively higher over the UV range.

To further investigate the performances of the ellipsometer, a series of standard SiO_2 films on the Si substrate are measured using the house-made MME. The nominal oxide layer thicknesses of the standard SiO_2/Si samples range from 2 nm to 1000 nm, including both thin and thick thin films, which gives comprehensive assessment of the performance of the ellipsometer. In the analysis, we use the mean squared error (MSE) to estimate the goodness of the fit between the model-calculated data and the experimental data. The MSE is defined as

$$MSE = \sqrt{\frac{1}{15N - M}\sum_{n=1}^{N}\sum_{i,j=1}^{4}(m_{ij,n}^{\exp} - m_{ij,n}^{\mathrm{calc}})^2} \times 1000, \quad (18)$$

where N is the total number of wavelengths, M is the total number of fit parameters in the optical model, n is the n-th spectral point from the total number N, indices i and j show all the Mueller matrix elements except m_{11} (normalized to m_{11}), and $m_{ij,n}^{\exp}$ and $m_{ij,n}^{\mathrm{calc}}$ denote measured and model-calculated Mueller matrix elements at the n-th spectral point, respectively. Thus, the MSE defined in equation (18) sums the differences between the model-calculated data and the measured data over the experimental spectral range. Since the precision in the normalized Mueller matrix elements measured by the house-made MME is ∼0.001 as shown above, a multiplicative factor 1000 is involved in the definition of MSE. This implies that the MSE for an ideal model fit should be ∼1.

Table 1. Measured results of the standard SiO_2/Si samples compared with their nominal values.

Number	Nominal Thickness (nm)	Measured Thickness (nm)	MSE
1	2	1.77 ± 0.0036	0.52
2	10	10.86 ± 0.0037	0.55
3	25	25.77 ± 0.0040	0.57
4	100	105.21 ± 0.0015	1.78
5	340	342.96 ± 0.0022	2.48
6	1000	1025.04 ± 0.0038	4.40

Figure 8 shows the results of the measured and best-fit Mueller matrix spectra for 2 nm and 1000 nm standard SiO_2 films. The measurements are performed at the reflective measurement mode with the incident angle of 60°, and the fitting thicknesses are 1.77 nm and 1025.04 nm for the thin and thick SiO_2 thin films, respectively. For standard SiO_2/Si samples, the two 2 × 2 off-diagonal blocks of the Mueller matrices are zero as shown in figure 8, while other elements can be expressed in terms of conventional ellipsometric angles Ψ and Δ [18], i.e., $m_{12} = m_{21} = -\cos 2\Psi$, $m_{34} = m_{43} = \sin 2\Psi \sin\Delta$, $m_{33} = m_{44} = \sin 2\Psi \cos\Delta$, $m_{22} = 1$. It can be observed from figure 8 that the best-fit Mueller matrix spectra demonstrate high agreement with the measured ones, and the fitting thicknesses of the SiO_2 samples are reasonable.

The measured results of the standard SiO_2/Si samples, including the mean thicknesses, their standard deviations and the mean values of the MSEs of 30 repeated measurements performed at the incident angle of 60°, are shown in table 1 compared with their nominal thicknesses. From table 1, it can

be seen that the measured thicknesses are reasonable for all the standard SiO_2/Si samples compared with their designed values, and standard deviations of the thicknesses are less than 0.004 nm, which belongs to a very high level of measurement repeatability for ellipsometers. It can be also observed that the MSEs are less than 5 for all the samples, which indicates high goodness of fit for both thin and thick SiO_2/Si samples. In addition, the MSE increases with the thicknesses of the films. The MSE of the 100 nm SiO_2/Si sample exhibits the closest level of the precision and accuracy of the MME. For the 2 nm, 10 nm and 25 nm SiO_2/Si samples, the MSEs are smaller than the level of the precision and accuracy, which implies that the fit results may include some random errors from the measured data. The MSEs may exhibit larger than the level of the precision and accuracy for complex samples, such as thick SiO_2 films, and this is still acceptable considering the complex spectral curves of the Mueller matrix elements as shown in figure 8(b).

6. Conclusions

In this work, a novel MME configuration based on dual rotating-GCW with flexibly oriented axes has been developed and optimized. Basic principles for data reduction and system calibration of the MME are presented. The ellipsometer is further optimized by a condition number related method. The optimization process of GCWs used for the corresponding MMEs over the wavelength range of 200~1000 nm is performed to verify the proposed method. Compared with the typical Pancharatnam waveplates and Becker's waveplates, the presented GCWs are not limited to specific structures, which provide many more flexibilities to adapt to the optimization of the MME. A house-made MME prototype based on optimally designed quartz triplates is developed to perform experiments. Experimental results on the air demonstrate that the house-made MME has an accuracy better than 0.2% and a precision better than 0.1% in the measurements of Mueller matrix elements over the wavelength range of 200~1000 nm. The house-made MME also exhibits high-level measurement repeatability better than 0.004 nm in testing the thicknesses of a series of standard SiO_2/Si films with nominal thicknesses ranging from 2 nm to 1000 nm. Compared with other MME devices, the proposed MME has advantages due to its great potential in broadband operation, convenience for system adjustment and calibration, and stable performance.

It is also worth pointing out that the MME based on quartz triplates over the wavelength range of 200~1000 nm is just taken as an example to demonstrate the great potential of the proposed method. The method itself is general and can be applied to optimally design a broadband MME with high measurement accuracy and precision over any wavelength range based on GCWs containing an arbitrary number of single waveplates.

Acknowledgments

This work was funded by the National Natural Science Foundation of China (51475191, 51405172, 51575214, and 51525502), the Natural Science Foundation of Hubei Province of China (2015CFB278 and 2015CFA005), the China Postdoctoral Science Foundation (2014M560607 and 2015T80791), and the Program for Changjiang Scholars and Innovative Research Team in University of China (IRT13017).

References

[1] Chen C, An I and Collins R W 2003 Multichannel Mueller matrix ellipsometry for simultaneousr real-time measurement of bulk isotropic and surface anisotropic complex dielectric functions of semiconductors *Phys. Rev. Lett.* **90** 217402
[2] Garcia-Caurel E, De Martino A, Gaston J P and Yan L 2013 Application of spectroscopic ellipsometry and Mueller ellipsometry to optical characterization *Appl. Spectrosc.* **67** 1
[3] Aspnes D E 2014 Spectroscopic ellipsometry—past, present, and future *Thin Solid Films* **571** 334
[4] Liu S, Chen X and Zhang C 2015 Development of a broadband Mueller matrix ellipsometer as a powerful tool for nanostructure metrology *Thin Solid Films* **584** 176
[5] Chen X, Liu S, Zhang C, Jiang H, Ma Z, Sun T and Xu Z 2014 Accurate characterization of nanoimprinted resist patterns using Mueller matrix ellipsometry *Opt. Express* **22** 15165
[6] Zhu J, Liu S, Jiang H, Zhang C and Chen X 2015 Improved deep-etched multilayer grating reconstruction by considering etching anisotropy and abnormal errors in optical scatterometry *Opt. Lett.* **40** 471
[7] Chen X, Zhang C, Liu S, Jiang H, Ma Z and Xu Z 2014 Mueller matrix ellipsometric detection of profile asymmetry in nanoimprinted grating structures *J. Appl. Phys.* **116** 194305
[8] Losurdo M and Hingherl K 2013 *Ellipsometry at the Nanoscale* (Berlin/Heidelberg: Springer)
[9] Azzam R M A 1978 Photopolarimetric measurement of the Mueller matrix by Fourier analysis of a single detected signal *Opt. Lett.* **2** 148
[10] Collins R W and Koh J 1999 Dual rotating-compensator multichannel ellipsometer: instrument design for real-time Mueller matrix spectroscopy of surfaces and films *J. Opt. Soc. Am.* A **16** 1997
[11] Chen C, An I, Ferreira G M, Podraza N J, Zapien J A and Collins R W 2004 Multichannel Mueller matrix ellipsometer based on the dual rotating compensator principle *Thin Solid Films* **455–456** 14
[12] Li J, Ramanujam B and Collins R W 2011 Dual rotating compensator ellipsometry: theory and simulations *Thin Solid Films* **519** 2725
[13] De Martino A, Kim Y K, Garcia-Caurel E, Laude B and Drevillon B 2003 Optimized Mueller polarimeter with liquid crystals *Opt. Lett.* **28** 616
[14] Aas L M S, Ellingsen P G, Fladmark B E, Letnes P A and Kildemo M 2013 Overdetermined broadband spectroscopic Mueller matrix polarimeter designed by genetic algorithms *Opt. Express* **21** 8753
[15] Jellison G E Jr and Modine F A 1997 Two-modulator generalized ellipsometry: theory *Appl. Opt.* **36** 8190
[16] Arteaga O, Freudenthal J, Wang B and Kahr B 2012 Mueller matrix polarimetry with four photoelastic modulators: theory and calibration *Appl. Opt.* **51** 6805

[17] Wang B, Hinds E and Krivoy E 2009 Basic optical properties of the photoelastic modulator: II. Residual birefringence in the optical element *Proc. SPIE* **7461** 746110
[18] Tompkins H G and Irene E A 2005 *Handbook of Ellipsometry* (New York: William Andrew Publishing)
[19] Smith M H 2002 Optimization of a dual-rotating-retarder Mueller matrix polarimeter *Appl. Opt.* **41** 2488
[20] Lee J, Rovira P I, An I and Collins R W 2001 Alignment and calibration of the MgF_2 biplate compensator for applications in rotating-compensator multichannel ellipsometry *J. Opt. Soc. Am.* A **18** 1980
[21] Arteaga O, Baldris M, Anto J, Canillas A, Pascual E and Bertran E 2014 Mueller matrix microscope with a dual continuous rotating compensator setup and digital demodulation *Appl. Opt.* **53** 2236
[22] Mawet D *et al* 2007 Fresnel rhombs as achromatic phase shifters for infrared nulling interferometry *Opt. Express* **15** 12850
[23] Kang T D, Standard E, Carr G L, Zhou T, Kotelyanskii M and Sirenko A A 2011 Rotatable broadband retarders for far-infrared spectroscopic ellipsometry *Thin Solid Films* **519** 2698
[24] Pancharatnam S 1955 Achromatic combinations of birefringent plates: II. An achromatic quarter-wave plate *Proc. Indian Acad. Sci.* **41A** 137
[25] Bechers J M 1971 Achromatic linear retarders *Appl. Opt.* **10** 973
[26] Hariharan P 1996 Achromatic and apochromatic halfwave and quarterwave retarders *Opt. Eng.* **35** 3335
[27] Hariharan P and Ciddor P E 2004 Broad-band superachromatic retarders and circular polarizers for the UV, visible and near infrared *J. Mod. Opt.* **51** 2315
[28] Hurwitz H Jr and Jones R C 1941 A new calculus for the treatment of optical systems: II. Proof of three general equivalence theorems *J. Opt. Soc. Am.* **31** 493
[29] Gu H, Liu S, Chen X and Zhang C 2015 Calibration of misalignment errors in composite waveplates using Mueller matrix ellipsometry *Appl. Opt.* **54** 684
[30] Chen X, Liu S, Gu H and Zhang C 2014 Formulation of error propagation and estimation in grating reconstruction by a dual-rotating compensator Mueller matrix polarimeter *Thin Solid Films* **571** 65
[31] Ichimoto K, Shinoda K, Yamamoto T and Kiyohara J 2006 Photopolarimetric measurement system of Mueller matrix with dual rotating waveplates *Publ. Natl. Astron. Obs. Japan* **9** 11
[32] Chandrasekhar S 1951 The dispersion and thermo-optic behaviour of vitreous silica *Proc. Indian Acad. Sci.* A **34** 275
[33] Dodge M J 1984 Refractive properties of magnesium fluoride *Appl. Opt.* **23** 1980
[34] Johs B 1993 Regression calibration method for rotating element ellipsometers *Thin Solid Films* **234** 395